Journal of The Electrochemical Society

Essential Role of Spinel $MgFe_2O_4$ Surfaces during Discharge

Journal of The Electrochemical Society, 2020 **167** 090506

Essential Role of Spinel $MgFe_2O_4$ Surfaces during Discharge

Haoyue Guo,[1] Jessica L. Durham,[1] Alexander B. Brady,[2] Amy C. Marschilok,[1,2,3,*] Esther S. Takeuchi,[1,2,3,] Kenneth J. Takeuchi,[1,2] and Ping Liu[1,4,z]**

[1]*Department of Chemistry, Stony Brook University, Stony Brook, New York 11794, United States of America*
[2]*Department of Materials Science and Chemical Engineering, Stony Brook University, Stony Brook, New York 11794, United States of America*
[3]*Energy and Photon Sciences Directorate, Brookhaven National Laboratory, Upton, New York 11793, United States of America*
[4]*Chemistry Department, Brookhaven National Laboratory, Upton, New York 11793, United States of America*

Spinel magnesium ferrite ($MgFe_2O_4$) is a prospective anode material in lithium ion battery (LIB) due to its large theoretical capacity. Here, we employed Density Functional Theory (DFT) to study the contribution from diverse facets of three spinel systems of $MgFe_2O_4$, normal-spinel, mixed-spinel and inverse-spinel, to the initial discharge behaviors. The mixed-spinel (1 0 0) surface terminated by $MgFeO_x$ is found to be the most active among the diverse surfaces studied. It can provide the high capacity, the high voltage and facile Li^+ transport during the initial discharge stage. The high performance is found to be associated with the high surface activity to capture Li^+ ions, and the ability to accommodate a large amount of Li^+ ions and facilitate the sequential smooth transport to subsurface. The DFT-estimated discharge voltages based on the mixed-spinel (1 0 0) surface terminated by $MgFeO_x$ are much higher than those using the stoichiometric bulk models and fit well with the corresponding experimental measurement at the initial stage. Our results develop new design strategies for optimization of particle morphologies, enabling the enhancement in stability and discharge performance of ferrite materials.

 [DOI: 10.1149/1945-7111/ab7f89]

Manuscript submitted February 10, 2020; revised manuscript received March 3, 2020. Published March 23, 2020. *This paper is part of the JES Focus Issue on Battery Safety, Reliability and Mitigation.*

Supplementary material for this article is available online

Spinel ferrites, AFe_2O_4 (e.g. A = Zn, Mg), are prospective anode materials in lithium ion battery (LIB), owing to their high theoretical capacity and natural abundance reserve. Nevertheless, these ferrite materials suffer from capacity fading upon cycling.[1–5] The improvement of rate performance and cyclability strongly depends on the fundamental understanding of the discharge/charge mechanism. In our previous studies, the Density Functional Theory (DFT) calculations successfully described the mechanism during the charge of spinel AFe_2O_4 bulks from AFe_2O_4 up to $Li_xAFe_2O_4$ (x = 2) and identified the key intermediates, which were able to reproduce the experimental measured open circuit voltages (OCVs) for $x \geqslant 0.5$.[2,3,5] However, the bulk models failed to describe the early discharge stage with $x < 0.5$, where the DFT-estimated OCVs were much lower than the corresponding experimental values. Such phenomena have been observed not only for $MgFe_2O_4$[5] and $ZnFe_2O_4$,[3,4] but also for Fe_3O_4[6] as well. The discrepancy in OCV was solved for $ZnFe_2O_4$ by including the contribution from the most stable $ZnFe_2O_4$(1 1 1) surface, where the stability of Li^+ ions was enhanced via the presence of the active ions with lower coordination than those in bulk.[4] In the present study, we move from $ZnFe_2O_4$ to $MgFe_2O_4$, which necessitates consideration of the increase in diversity of spinel going from a single normal-spinel as the case of $ZnFe_2O_4$ to three spinel structures, including normal-spinel, mixed-spinel and inverse-spinel for the $MgFe_2O_4$ system.[1,5,7]

Bulk $MgFe_2O_4$ is not limited to normal-spinel (O^{2-}: octahedral 32e; Fe^{3+}: octahedral 16d; Mg^{2+}: tetrahedral 8a sites) as the case of $ZnFe_2O_4$; Rather, it can also adopt mixed- and inverse-spinel structures, where 16d Fe^{3+} ions partially or completely intermix with 8a Mg^{2+} ions depending on synthesis methods.[8–16] As a consequence, the preferential surface orientations also vary from dominant (1 1 1) in normal-spinel $ZnFe_2O_4$ to the combination of (1 0 0) and (3 1 1) in normal-spinel, {1 0 0} in mixed-spinel and a combination of (1 0 0), (0 0 1), (1 1 1) and (3 1 1) in inverse-spinel of $MgFe_2O_4$ according to our previous study.[7] However, all the stable surfaces feature a high density of stable Mg^{2+} ions exposed to the surface, which significantly lowers the surface energy. The impact on the capture of Li^+ ions on these surfaces and the differences in transport properties from surface to bulk are still underexplored and deserve considerable attentions.

Here, building on our previous studies of pristine $MgFe_2O_4$ surfaces,[7] we investigated the adsorption and transport of the Li^+ ions on the stable facets of three spinel structures using DFT: (1 0 0) and (3 1 1) in normal-spinel, {1 0 0} in mixed-spinel and (1 0 0), (0 0 1), (1 1 1) and (3 1 1) in inverse-spinel. These DFT-identified surfaces agreed well with previous high-resolution transmission electron microscope (HR-TEM) results.[17–23] Our DFT calculations enabled the identification of the most active surface orientation, capable of enhancing the capacity, discharge voltage and Li^+ ion transport from surface to bulk. More importantly, it provided mechanistic understanding of the origin for the superior activity and offered new design strategies to optimize the particle morphologies and thus enhance the discharge performance of ferrite materials.

Experimental

DFT Calculations.—DFT implemented in the Vienna ab initio simulation package (VASP)[24,25] was employed. The spin-polarized DFT+U calculations[26–28] were carried out with the PAW potential[25,29] using the PBE exchange-correlation functional[30] and a kinetic energy cutoff of 520 eV. A Hubbard U correction of $U_{eff} = 5.3$ eV was applied to the Fe d orbitals. This setup was successfully used to predict the discharging properties observed experimentally for bulk and surface $MgFe_2O_4$ according to our previous studies.[5,7] The Gaussian smearing method was used with the total energies converged better than 10^{-5} eV, and the final force on each atom is less than 0.02 eV $Å^{-1}$. The first Brillouin zone was sampled on 3 × 3 × 1 k-mesh. The 2 × 2 slab model was constructed to describe various $MgFe_2O_4$ surfaces. A 20 Å thick vacuum was added along the direction perpendicular to the surface to avoid the artificial interactions between the slabs. During geometry optimization, the

*Electrochemical Society Member.
**Electrochemical Society Fellow.
[z]E-mail: pingliu3@bnl.gov

top three layers were allowed to relax with adsorbed Li^+ ions, while the rest were fixed at the bulk position.

The supercell of $MgFe_2O_4$ bulk was constructed with the Fd $\bar{3}$ m primitive cell containing eight formula units in normal-spinel, mixed-spinel and inverse-spinel structures. According to the previous synchrotron X-ray powder diffraction (XPD) measurement,[5] for the mixed-spinel structure, the formula of $(Mg_{0.25}Fe_{0.75})_{8a}(Mg_{0.75}Fe_{1.25})_{16d}O_4$ with the inversion degree of 0.75 was constructed. The DFT-optimized lattice parameters of 8.54 Å, 8.52 Å, 8.50 Å in normal-spinel, mixed-spinel and inverse-spinel, respectively (8.40 Å in experiments[5,8,14]); and band gaps of 1.5 eV (1.5 ∼ 2.0 eV in experiments[16,17,31]) in three systems are in reasonable agreement with the values measured experimentally.

Discharge calculations.—The Li adsorption/binding energy is defined as[32]

$$E_b = E_{xLi/Surface} - E_{Surface} - xE_{Li^+}$$

where $E_{xLi/Surface}$, $E_{Surface}$, and E_{Li+} correspond to the total energy of Li-adsorbed surface, bare surface and aqueous Li^+ ion, respectively. x is the number of Li on the surface. Negative E_b represents an energetically favorable adsorption.

The average intercalation voltage is calculated by[33]

$$V = -\frac{E_{xLi/Surface} - E_{Surface} - xE_{Li}}{xF}$$

where E_{Li} stands for the total energy of Li bulk and F is Faraday's constant.

General methods and materials.—Magnesium ferrite was synthesized via a combination of co-precipitation and hydrothermal reaction with a subsequent calcination step modified from previously reported schemes.[34–36] Magnesium(II) nitrate, iron(III) nitrate, and sodium hydroxide reagents were used as received. The dry material was annealed in a tube furnace at 400 °C. X-Ray powder diffraction (XRD) of $MgFe_2O_4$ was collected with a Rigaku SmartLab X-ray diffractometer utilizing Cu Kα radiation, a Scintillation detector, and Bragg-Brentano focusing geometry. The XRD spectra were measured in a 2θ range from 5° to 90°. Rigaku PDXL2 software and the ICDD PDF-2 database was used for search-match analysis to identify the composition of the prepared material. Magnesium ferrite crystallite sizes were approximated by applying the Scherrer equation to the (3 3 1) reaction at a 2θ value of approximately 35° in the XRD pattern.

Coin-cell type batteries with lithium anodes were used to probe the electrochemistry of $MgFe_2O_4$, under an applied current density of 100 mA g^{-1} between 0.2 and 3.0 V vs lithium. Galvanostatic measurements utilized $MgFe_2O_4$ electrodes prepared with 85% active material, 10% Super P carbon black, and 5% binder on a copper foil substrate. An electrolyte solution of 1 M $LiPF_6$ in 30/70 (*v*/*v*) ethylene carbonate/dimethyl carbonate solution was used. Electrochemical tests were done on two—electrode coin type cells assembled in an Ar-filled glove box with lithium as the counter electrode, polymer separator, and the $MgFe_2O_4$ working electrode.

Results and Discussion

Initial Li^+ adsorption.—Li^+ ions were employed as a probe to evaluate the binding capability of each stable surface identified previously for pristine $MgFe_2O_4$.[7] The adsorption of Li^+ was considered at a low coverage, which described the situation at the very initial stage of discharge.

Normal-spinel $MgFe_2O_4$.—The stable (1 0 0) surfaces terminated by Mg or FeO_2, (1 0 0)-Mg or (1 0 0)-FeO_2 in our notation, and (3 1 1)-O or (3 1 1)-MgO_4 surfaces were considered for Li^+ ion adsorption on pristine normal-spinel $MgFe_2O_4$, according to our previous study.[7] Here, the topmost surface composition was used to label the surface termination. Various surface oxygen sites were tested (Figs. 1 and S1–S2 is available online at stacks.iop.org/JES/167/090506/mmedia). On (1 0 0)-Mg (Figs. 1a and S2), all the oxygen sites are able to provide the strong bindings to Li^+ ion, among which the O_1O_2-Bridge site with the binding energy (E_b) of −2.59 eV (Table I), is the most favorable. The highly negative E_b indicates a strong thermodynamic preference to capture the Li^+ ion from solution by (1 0 0)-Mg. However, this is not the case for (1 0 0)-FeO_2 (Figs. S1–S2), where the positive E_b for all surface oxygen sites are observed. The most preferred O_5O_6-Bridge site corresponds to E_b as high as 0.97 eV (Table I). That is, thermodynamically (1 0 0)-FeO_2 is not likely to attract the Li^+ ion. In both cases, the Li^+ ion interacts with two oxygen on adsorption. The difference is the local environment of the adsorption site. Compared to (1 0 0)-FeO_2, more Mg^{2+} ions are exposed on (1 0 0)-Mg (Figs. 1a and S2), which promotes the surface stability via the strong Mg-O interaction as shown previously.[7] In the meantime, it also weakens the Fe-O bond on the surface. Upon discharge, Li is the electron donor. With the formation of Li–O bonds on the surfaces, one electron is transferred from Li to the surface, which is demonstrated by the limited states of Li 2 s and 2p right below the Fermi level according to the projected density of states (PDOS, Fig. 2a). As a result, the surface

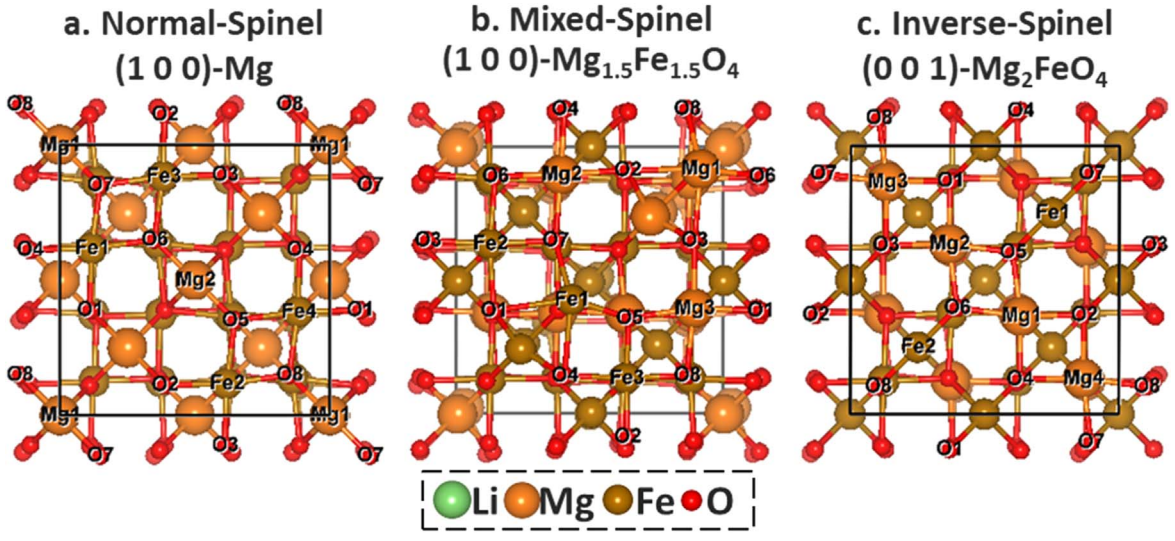

Figure 1. Top view of the active bare $MgFe_2O_4$ surfaces of normal-spinel (1 0 0)-Mg (a), mixed-spinel (1 0 0)-$Mg_{1.5}Fe_{1.5}O_4$ (b) and inverse-spinel (0 0 1)-Mg_2FeO_4 (c). The ions exposed to surface were labeled.

Table I. Lowest Li^+ ion adsorption/binding energies E_b (eV) for various surface terminations in normal-, mixed- and inverse-spinel.

Crystal	Surface Termination	Binding Energy E_b (eV)
Normal	(1 0 0)-Mg	−2.59
	(1 0 0)-FeO_2	0.97
	(3 1 1)-O^1	1.13
	(3 1 1)-O^2	0.38
	(3 1 1)-MgO_4	−2.21
Mixed	(1 0 0)-$Mg_{1.5}Fe_{1.5}O_4$	−8.81
	(0 0 1)-MgO_2	−7.51
	(0 0 1)-FeO_2	−3.91
Inverse	(1 0 0)-$MgFeO_4$	−3.37
	(0 0 1)-Mg_2FeO_4	−6.07
	(1 1 1)-O	−4.91
	(3 1 1)-O	−3.96

Fe^{3+} ions (Fe1–4, Fig. 1a), which interact directly to either O_1 or O_2 on the surface, are partially reduced to Fe^{2+}, as the conduction bands are dominated by Fe 3d states with little contribution from Li^+ and Mg^{2+}.[7] Consequently, the binding to Li^+ ion is strengthened due to the weakened electrostatic repulsion from the Fe^{2+} ions as compared to Fe^{3+}. However, little change was observed for (1 0 0)-FeO_2 (Fig. 2b) on Li^+ ion. That is, the Fe^{3+} ions next to the O_5O_6-Bridge remains as 3 + instead. The strong repulsive force from Fe^{3+} hinders the approach of Li^+ ion to the surface. In this case, the electron donated by intercalated Li results in the reduction of Fe^{3+} in the subsurface instead, so that the strong Fe^{3+}–O^{2-} bonds on the surface and thus lower the surface energy can be sustained. For the same reason, all the adsorption sites on (1 0 0)-Mg can provide much stronger binding than that on (1 0 0)-FeO_2.

The essential role of Mg^{2+} ions in enhancing the Li^+ adsorption is also observed on (3 1 1) surfaces. Among the stable (3 1 1) surfaces with three different terminations, featured with the highest density of surface Mg^{2+} ions all oxygen sites on (3 1 1)-MgO_4 can provide strong bindings to the Li^+ ion (Figs. S1–S2). Wherein, the most favorable is the $O_1O_7O_{12}$-Hollow(16c-Vacancy) site (E_b = −2.21 eV, Table I). When the surfaces are terminated by oxygen, neither the O-poor (3 1 1)-O^1 (E_b = 1.13 eV, Table I) nor the O-rich (3 1 1)-O^2 (E_b = 0.38 eV, Table I) favors the Li^+ adsorption. The increased amount of O^{2-} ions on the surface, however, helps the binding by enhancing the symmetry of adsorption site from 2-fold to 3-fold. Among the five stable facets of normal-spinel $MgFe_2O_4$, only (1 0 0)-Mg and (3 1 1)-MgO_4 surfaces are active for adsorption of initial Li^+ ions. Our results indicate that high density of Mg^{2+} ions exposed to the surface can strengthen the binding to the Li^+ ions in addition to improve the surface stability as reported previously.[7]

Mixed-spinel $MgFe_2O_4$.—For pristine mixed-spinel $MgFe_2O_4$, only the low-index (1 0 0)- $Mg_{1.5}Fe_{1.5}O_4$ and (0 0 1)-MgO_2, -FeO_2 surfaces are stable as shown previously (Figs. 1b and S1).[7] On (1 0 0)-$Mg_{1.5}Fe_{1.5}O_4$ (Fig. 1b), the 16c-Vacancy site is highly favored for the Li^+ adsorption (E_b = −8.81 eV). In the case of (0 0 1)-MgO_2 (Fig. S1), the Li^+ ion can be stabilized at the O_5O_8-Bridge site (E_b = −7.51 eV, Table I); by comparison without the presence of surface Mg^{2+}, the Li^+ adsorption at the O_5O_7-Bridge of (0 0 1)-FeO_2 (Figs. S1, S3) is much weaker (E_b = −3.91 eV, Table I). Again, the change of the termination from −FeO_2 to −MgO_2 results in a significant increase in Li^+ binding activity, confirming the promotion of surface Mg^{2+} ions on the Li^+ adsorption as seen in the case of normal-spinel $MgFe_2O_4$.

Inverse-spinel $MgFe_2O_4$.—The pristine inverse-spinel $MgFe_2O_4$ has the most diversity in stable facets,[7] all of which can stabilize the Li^+ ions according to the current DFT calculations. With the presence of Mg^{2+} ions on (0 0 1)-Mg_2FeO_4 surface (Fig. 1c), the Li^+ ion strongly interacts with the 16c-Vacancy site (E_b = −6.07 eV, Table I). While the binding is weakened with the decrease in surface Mg^{2+}, going from the 16d-Vacancy site of (1 1 1)-O (E_b = −4.91 eV, Figs. S1, S4), the $O_6O_7O_{10}$-Hollow site (16c-Vacancy) of (3 1 1)-O (E_b = −3.96 eV, Figs. S1, S4) to the O_3O_7-Bridge site of (1 0 0)-$MgFeO_4$ (E_b = −3.37 eV, Figs. S1, S4). Here, we note that the variation from normal-spinel to inverse-spinel modifies the surface activity of (3 1 1)-O facets, making it energetically favorable for initial Li^+ ion adsorption.

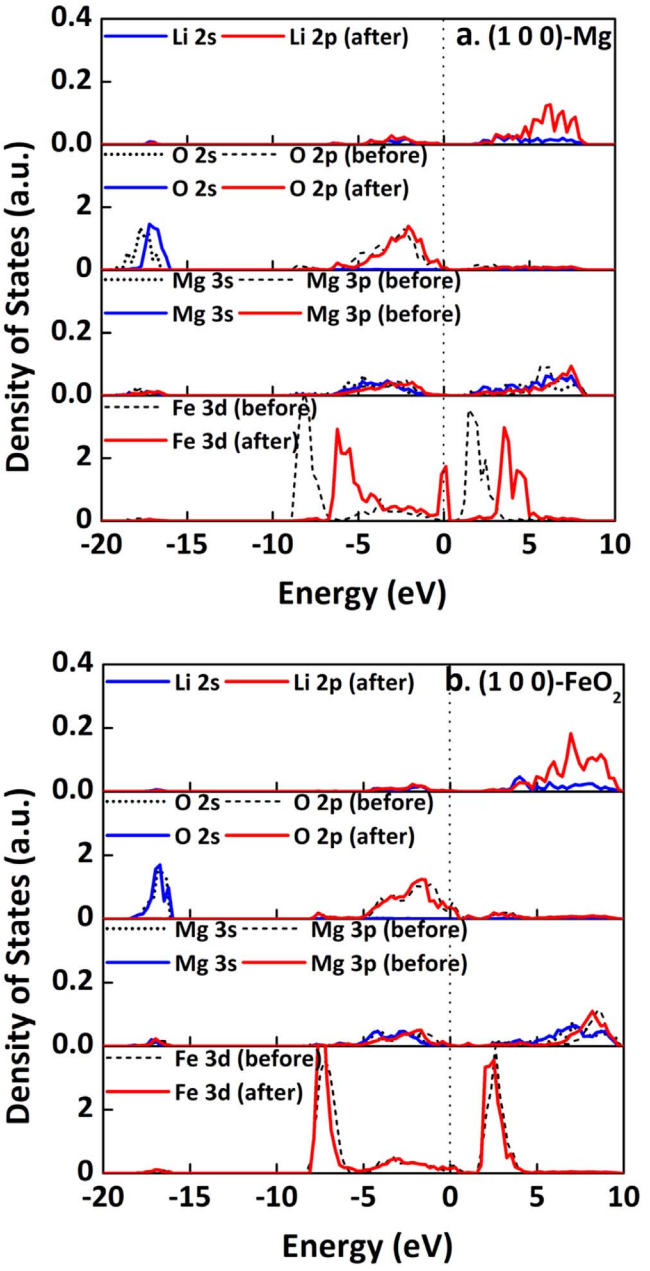

Figure 2. Projected density of states (PDOS) of surface ions before and after adsorption of Li^+ ion at the low coverage on normal-spinel $MgFe_2O_4$(1 0 0)-Mg (a) and (1 0 0)-FeO_2 (b).

Our DFT calculations show that like the case of $ZnFe_2O_4$,[4] the stability of $MgFe_2O_4$ surfaces correlates well with the capability to capture Li^+ ions. As demonstrated previously, the high surface stability depends on the dense Mg^{2+} ions exposed to the surface.[7] Accordingly, the statistics on densities of ions exposed for all the stable surfaces was performed, where a clear linear relationship between the density of Mg^{2+} ions and Li^+ ions binding energy was

observed (Fig. 3). That is, the higher density of Mg^{2+} ions correspond to the lower E_b or the higher capability to capture Li^+ ions. While no clear correlation is observed between E_b and the densities of both Fe^{3+} and O^{2-} ions (Fig. S5). For each phase of $MgFe_2O_4$, the most active surfaces for Li^+ ion capture feature the high Mg^{2+} ions density: 2.74 Mg nm^{-2} for (1 0 0)-Mg of normal-spinel, 4.13 Mg nm^{-2} for (1 0 0)-$Mg_{1.5}Fe_{1.5}O_4$ of mixed-spinel, and 5.54 Mg nm^{-2} for (0 0 1)-Mg_2FeO_4 of inverse-spinel (Fig. 4 and Table I). The origin of the promoting effect is associated with the strong ionic nature of Mg-O bond. It enables the stabilization of the surface oxygen and thus the surface on one hand; on the other hand, the electrostatic repulsion from the surface to the approaching of Li^+ ions is decreased by the preferential reduction of surface Fe^{3+} to Fe^{2+} during discharge, which enhances the capability of the surface to capture Li^+ ions.

In addition to the density of surface Mg^{2+}, the symmetry of oxygen sites for adsorption can also affect Li^+ binding. In mixed-spinel, although (0 0 1)-MgO_2 features higher density of surface Mg^{2+} ions (5.51 Mg nm^{-2}) than (1 0 0)-$Mg_{1.5}Fe_{1.5}O_4$, there is no highly O-coordinated octahedral 16c-Vacancy sites on/near surface and results in weaker binding to the Li^+ ions. A similar situation is also observed for inverse-spinel, where the 16d-Vacancy site on (1 1 1)-O with the higher density of surface Mg^{2+} ions (6.40 Mg nm^{-2}) is less active than that on (0 0 1)-Mg_2FeO_4 (Table I). The 16d-Vacancy site on (1 1 1)-O is located closer to Fe^{3+} ions than that on (0 0 1)-Mg_2FeO_4, which also contributes to the weakened Li^+-surface interaction. Nevertheless, neither the site symmetry nor the distance to the neighboring Fe^{3+} as significant as the density of surface Mg^{2+} ions in determining the capability for the Li^+ capture.

Li^+ saturation and discharge behavior.—As the discharge progresses, more and more Li^+ ions can be captured by the surfaces of $MgFe_2O_4$. Accordingly, we now extend our DFT calculations to study the sequential adsorption of Li^+ ions on surfaces from low to high coverage. For each type of spinel $MgFe_2O_4$, only the surface that is the most active to bind Li^+ ion was considered: (1 0 0)-Mg in normal-spinel, (1 0 0)-$Mg_{1.5}Fe_{1.5}O_4$ in mixed-spinel and (0 0 1)-Mg_2FeO_4 in inverse-spinel (Fig. 4).

Normal-spinel $MgFe_2O_4$.—On normal-spinel $MgFe_2O_4$(1 0 0)-Mg, the initial adsorption of Li^+ ion at coverage of 1.37 li nm^{-2} prefers the O_1O_2-Bridge site (Fig. 4). The additional Li^+ ion at the equivalent O_1O_2-Bridge site is energetically favorable with an increase in energy gain going from 2.59 eV to 3.48 eV at coverage of 2.74 li nm^{-2}. Starting at 4.11 li nm^{-2}, the preferential adsorption position varies from the Bridge site to Hollow site, which increases the exothermicity to −4.74 eV. This is also accompanied with surface distortion, where the Fe ions on surface and in sublayers shift from the octahedral 16d sites to the less stable tetrahedral vacancies (Fig. 4). The saturation coverage of Li^+ ions is 5.48 li nm^{-2} corresponding an energy gain of 6.06 eV. After saturation, the adsorption of additional Li^+ ion is hindered, which costs the energy of 4.01 eV. This is due to the strong repulsion from the existing Li^+ ions on the surface. Moreover, the significant structural distortion under high Li^+ coverage also indicates that the (1 0 0)-Mg surface of normal-spinel $MgFe_2O_4$ is not stable during the Li^+ adsorption process and may lead to low cyclability.

Mixed-spinel $MgFe_2O_4$.—On (1 0 0)-$Mg_{1.5}Fe_{1.5}O_4$, the active 16c-Vacancy site has already been occupied at coverage of 1.38 li nm^{-2}; while at 2.75 li nm^{-2} the additional Li^+ ions are forced to adsorb at the less active 16c-Vacancy sites which are closer to Fe^{3+} ions (Fig. 4). This is a slightly endothermic process, with a low energy cost of 0.08 eV. The further increase in coverage to 5.51 li nm^{-2} with Li^+ ions filled in the O_4O_5-Bridge site is thermodynamically preferred with energy release of 10.57 eV (Fig. 4). The adsorption at coverage of 6.89 li nm^{-2} is not likely corresponding to an energy cost of 0.64 eV and the increase in structural distortion,

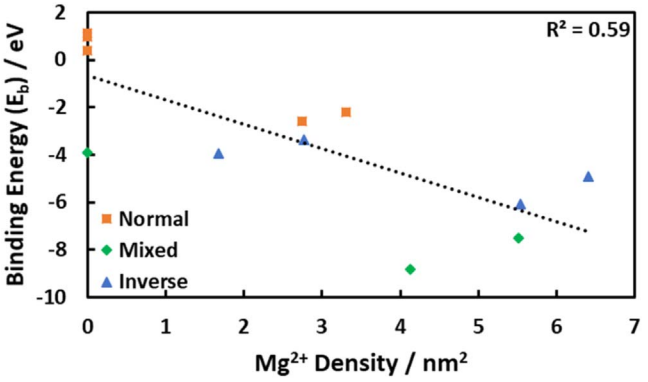

Figure 3. Correlation between Li^+ binding energy E_b (eV) and Mg^{2+} density per nm^2 exposed to the $MgFe_2O_4$ surfaces.

which is again associated with the lateral repulsion from the neighboring adsorbed Li^+ ions. Accordingly, the (1 0 0)-$Mg_{1.5}Fe_{1.5}O_4$ surface can be saturated by Li^+ ions up to coverage of 5.51 li nm^{-2}, where the active 16c-Vacancy and O_4O_5-Bridge sites are all occupied. Here, we assume the highly exothermic adsorption of Li^+ ions at 1.38 li nm^{-2} (−8.81 eV) likely overcome the small endothermicity (0.08 eV) to reach the coverage of 2.75 li nm^{-2}. During this process, the Fe^{3+} ion in subsurface is very mobile, displacing from the tetrahedral 8a site to octahedral 16c-Vacancy in the 1st sublayer and partially blocking the typical 16c → 16c pathway for Li^+ transport from surface to bulk.

Inverse-spinel $MgFe_2O_4$.—On (0 0 1)-Mg_2FeO_4 surface, the Li^+ ions locate at the 16c-Vacancy site at coverage of both 1.38 li nm^{-2} and 2.77 li nm^{-2}, with the energy gain of 6.07 eV and 8.88 eV, respectively (Fig. 4). After the 16c-Vacancy sites are saturated, the O_2O_4-Bridge sites are occupied by Li^+ ions at coverage of 4.15 li nm^{-2} and 5.54 li nm^{-2}, which is unlikely to occur due to the endothermicity of 1.92 eV and 3.64 eV, respectively. Thus, the saturation coverage in this case is as low as 2.77 li nm^{-2}.

The capability of three spinel $MgFe_2O_4$ surfaces to capture Li^+ is different. Both the mixed-spinel (1 0 0)-$Mg_{1.5}Fe_{1.5}O_4$ and inverse-spinel (0 0 1)-Mg_2FeO_4 with higher density of Mg^{2+} ions exposed to the surface are able to bind Li^+ more strongly than normal-spinel $MgFe_2O_4$(1 0 0)-Mg surface ranging from the low Li coverage to the saturated coverage (Fig. 4). This is also demonstrated by the PDOS (Figs. 2 and 5). More obvious change in Fe 3d state on discharge is observed as compared to that for other ions on the surface when going from mixed- and inverse-spinel to normal-spinel. Specifically, the delocalization of surface Fe 3d states is enhanced when the Li^+ ions are adsorbed on mixed-spinel (1 0 0)-$Mg_{1.5}Fe_{1.5}O_4$ (Fig. 5a) and inverse-spinel (0 0 1)-Mg_2FeO_4 (Fig. 5b). That is, the reduction of surface Fe^{3+} and thus the binding of Li^+ ions can be promoted on phase transition of $MgFe_2O_4$ from normal to mixed or inverse spinel. In term of saturation coverage, though, the inverse-spinel surface cannot accommodate Li^+ ions as much as that for normal- and mixed-spinel surfaces (Fig. 4). Overall, among the three phases of $MgFe_2O_4$ the mixed spinel is likely the most active, where the active (1 0 0)-$Mg_{1.5}Fe_{1.5}O_4$ surface not only allows active capture of Li^+ ions and thus likely high discharge voltage at the initial stage, but also enables the accumulation of Li^+ ions at high coverage, and thus likely high capacity. However, compared to $ZnFe_2O_4$ surfaces (12.66 li nm^{-2}),[4] the saturation coverage (up to 5.51 li nm^{-2}) for $MgFe_2O_4$ is significantly lower. The high density of Mg^{2+} ions in $MgFe_2O_4$ does improve initial Li^+ ions adsorption with lower E_b in comparison with $ZnFe_2O_4$ ($E_b < -5$ eV); however, the drawback is that the existing surface Mg^{2+} ions block some of the active sites for adsorption, and limits the high saturation by Li^+ ions.

To evaluate the contribution of Li^+ adsorption on the surfaces to the discharge of $MgFe_2O_4$, the DFT-calculated E_b (Fig. 4) on the stable surfaces were used to estimate the average cell voltages. Here,

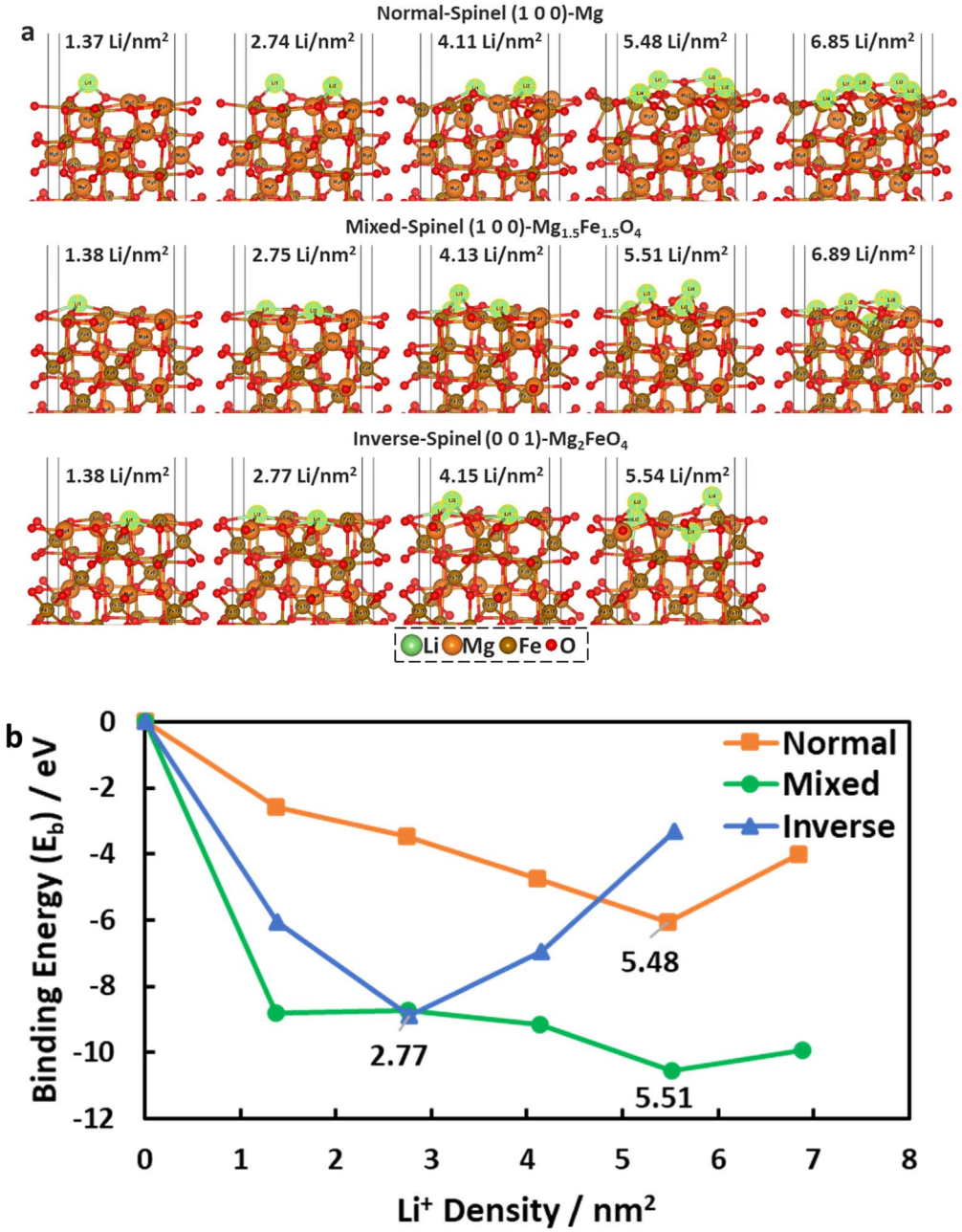

Figure 4. Variation in structures (a) and binding energy (E_b) for Li^+ ion adsorption on normal-spinel $MgFe_2O_4$(1 0 0)-Mg, mixed-spinel (1 0 0)-$Mg_{1.5}Fe_{1.5}O_4$ and inverse-spinel (0 0 1)-Mg_2FeO_4 with the density of Li^+ ions on the surface.

the active $MgFe_2O_4$ in mixed spinel was taken as a case study. Using the bulk model,[5] it was shown previously that the DFT-estimated discharge voltage agreed reasonably well with the experimental value at $x > 0.5$ (Fig. 6); however, at $x < 0.5$ the theoretical estimation is much lower, particularly at the very early stage with $x < 0.25$. Following our previous study of $ZnFe_2O_4$ surfaces,[4] the coverage of Li^+ on the surface was converted to the x value in the form of $Li_xMgFe_2O_4$, according to the number of Li^+ ions adsorbed and therefore the number of electrons transferred in addition to the corresponding surface areas for the particles measured experimentally.[5] Our results show that at $x < 0.25$ the estimated discharging voltage based on the DFT-calculated E_b for mixed-spinel (1 0 0)-$Mg_{1.5}Fe_{1.5}O_4$ are much higher than that based on the bulk materials and describes well the experimental measurements (Fig. 6). Such an observation again confirms the important contribution from surfaces to the initial lithiation as seen for $ZnFe_2O_4$ surfaces.[7] Compared to bulk, the surface is able to provide the lower-coordinated oxygen sites for Li^+ and enable the less structural distortion driven by intercalated Li^+ ions, which help in enhancing the stability of intercalated Li^+ ions.

To experimentally verify the voltage profile, $MgFe_2O_4$ material was synthesized and electrochemically evaluated. X-ray powder diffraction was consistent with a $MgFe_2O_4$ spinel ($Fd\bar{3}m$) reference pattern indicating no crystalline impurities. A crystallite size of 10 nm was determined by applying the Scherrer equation[37,38] to the (3 3 1) reflection at a 2θ value of approximately 35°. Rietveld refinement showed good agreement of lattice parameters compared to crystalline $MgFe_2O_4$ group (8.3674 Å)[39] and our DFT calculations (8.52 Å), with a = b = c of 8.7345[9] Å and an R_{wp} of 0.76% (Fig. S7). The material was electrochemically evaluated in two electrode cells. The voltage profile showed a difference in cycle 1, with consistent profiles for cycles 5 and 10 (Fig. 7a). The cycle 1

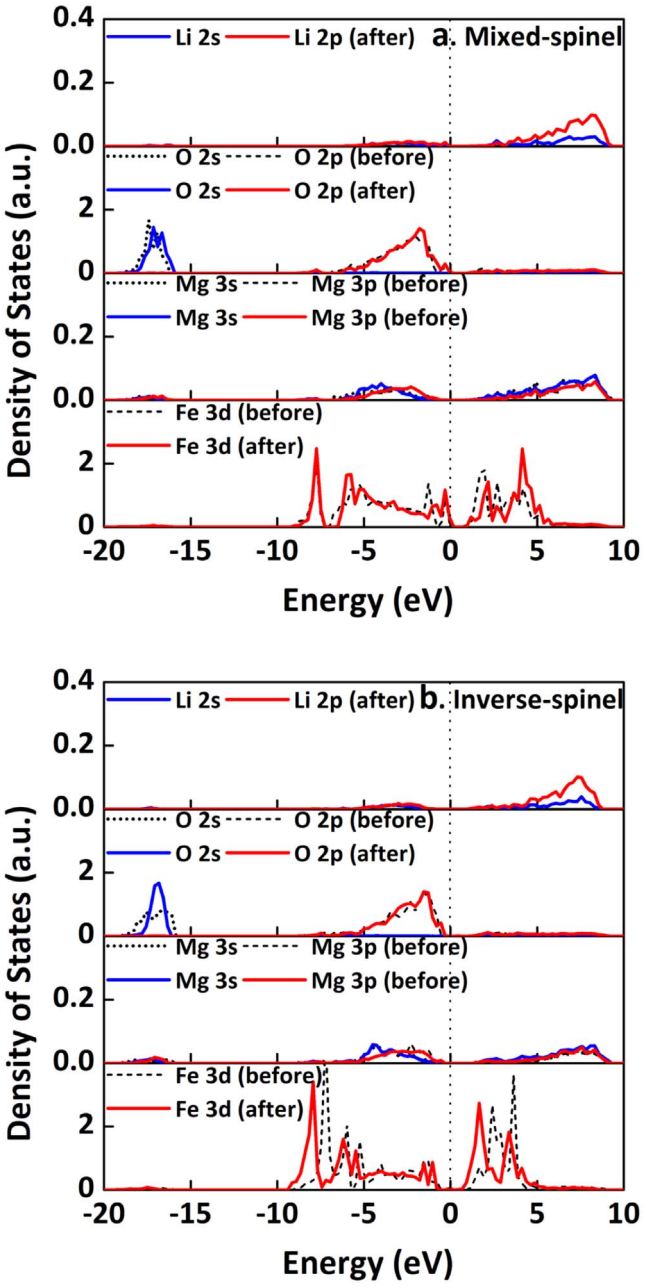

Figure 5. Projected density of states (PDOS) of surface ions before and after adsorption of Li^+ at the low coverage on mixed-spinel $MgFe_2O_4$(1 0 0)-$Mg_{1.5}Fe_{1.5}O_4$ (a) and inverse-spinel (0 0 1)-Mg_2FeO_4 (b).

discharge capacity exceeded the theoretical capacity of $MgFe_2O_4$, 804 mAh g^{-1}, with values above 1200 mAh g^{-1}. The excess cycle 1 capacity is attributed to the decomposition of the electrolyte and the formation of the SEI and Li_2O on the surface of the pristine electrode at the electrolyte interface, a process that coincides with the irreversible capacity loss between cycles 1 and 2.[20,40–44] Subsequent cycle discharge capacities realized were ~85% of the theoretical capacity (Fig. 7b).

Li^+ transport from surface to subsurface.—Besides the Li^+ capture, the transport from surface toward bulk is also key to the discharge performance. To gain better understanding, we investigated Li^+ ion transport from surface to subsurface on three stable and active surfaces, normal-spinel $MgFe_2O_4$(1 0 0)-Mg, mixed-spinel $MgFe_2O_4$(1 0 0)-$Mg_{1.5}Fe_{1.5}O_4$ and inverse-spinel (0 0 1)-Mg_2FeO_4. Three sublayers, 1st, 2nd, and 3rd sublayers in addition to the surface layer, were defined (Fig. S6) to open a path for Li^+ transport. Finally, both low and saturated coverage of Li^+ ions were considered to account for the coverage effect (Figs. 8 and S8–S9).

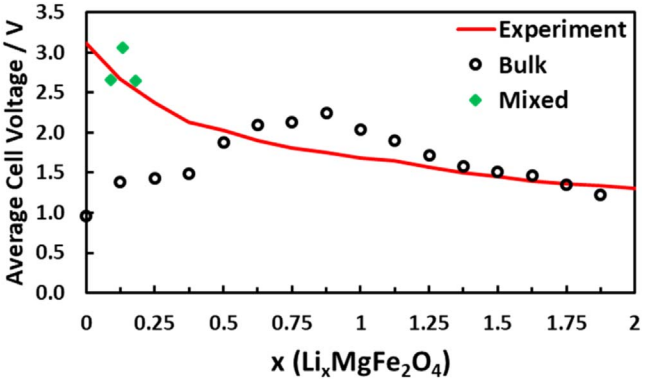

Figure 6. DFT-estimated average cell voltages based on mixed-spinel $MgFe_2O_4$ bulk models and (1 0 0)-$Mg_{1.5}Fe_{1.5}O_4$ surface models in comparison with experimentally measured operating voltage circuit. The bulk data points using DFT and the experimental results were cited from Bock, et al.[5]

Normal-spinel $MgFe_2O_4$.—At low coverage, (1 0 0)-Mg is too stable to allow the Li^+ transport from the O_1O_2-Bridge on the surface to the 16c position of the 1st sublayer, which shifts back to surface site after geometry optimization (Figs. 8a, 8b). The following Li^+ transport to 16c-Vacancy site in the 2nd sublayer (Fig. 8c) is also unfavorable, with an energy loss of 4.23 eV. From the 2nd to the 3rd sublayer (Fig. 8d) the process is energetically preferred with an energy gain of 2.73 eV. That is, at low coverage the Li^+ ion transport is very unlikely from the normal-spinel $MgFe_2O_4$(1 0 0)-Mg surface to bulk. When comparing the energetics, the surface saturation by Li^+ ions is more favorable than the Li^+ transport (Fig. 4). That is, Li^+ ions prefer to accumulate on the surface at the initial lithiation stage to a saturated coverage prior to the transport to subsurface, as we observed in previous study in $ZnFe_2O_4$.[4] On the saturated (1 0 0)-Mg (Fig. 8e), the adsorption of additional Li^+ ions is hindered due to the electrostatic repulsion from the saturated Li^+ ions (Fig. 8f) and the corresponding binding energy is positive (E_b = 2.05 eV); however, it facilitates the transport toward the 2nd sublayer (Fig. 8g) corresponding to an energy gain of 4.90 eV; while the further displacement toward the 3rd sublayer (Fig. 8h) costs energy of 2.29 eV. Nevertheless, the transport of Li^+ ions from the Li^+-saturated surface is thermodynamically more feasible than that from the bare surface (Fig. 8).

Mixed-spinel $MgFe_2O_4$.—At low coverage, the initial adsorption of Li^+ ion at the octahedral 16c-Vacancy site at the 1st sublayer is favorable with an energy gain of 8.81 eV (Figs. 8 and S6a, S6b). The further transport to the 2nd sublayer (Fig. S6c) is also exothermic by 1.45 eV. During this process, the transport from the 2nd sublayer to the 3rd sublayer (Fig. S6d) is the only endothermic step, which costs energy of 3.00 eV. Thus, at low coverage the Li^+ ion transport along the mixed-spinel $MgFe_2O_4$(1 0 0)-$Mg_{1.5}Fe_{1.5}O_4$ surface is likely feasible, driven by the significant energy gain in adsorption and transport to the 2nd sublayer. On the Li^+-saturated surface, which is more likely to occur than transport according to the energetics (Figs. 4 and 8), the existing Li^+ ions occupy all the active surface sites (Fig. S6e). Yet, he sequential adsorption (0.64 eV, Fig. S6f), the transport from surface to the 2nd sublayer (−3.98 eV, Fig. S6g) and from the 2nd to the 3rd sublayer (2.27 eV, Fig. S6h) likely proceeds smoothly with no highly endothermic step involved (Fig. 8).

Inverse-spinel $MgFe_2O_4$.—The Li^+ transport along (0 0 1)-Mg_2FeO_4 surface shows similar behavior as mixed-spinel (1 0 0)-$Mg_{1.5}Fe_{1.5}O_4$ (Figs. 8 and S8) under both the low coverage and

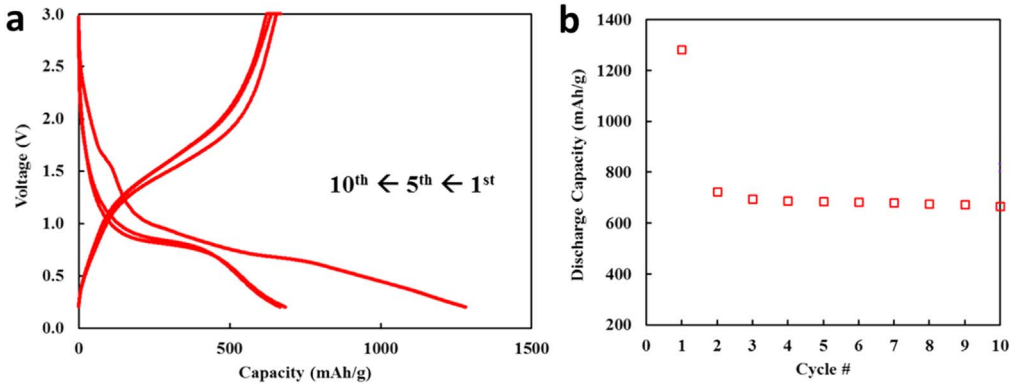

Figure 7. Discharge and charge of Li/$MgFe_2O_4$ cells between 0.1−3.0 V (a) Voltage curves for cycles 1, 5, and 10. (b) Discharge capacities for cycles 1–10.

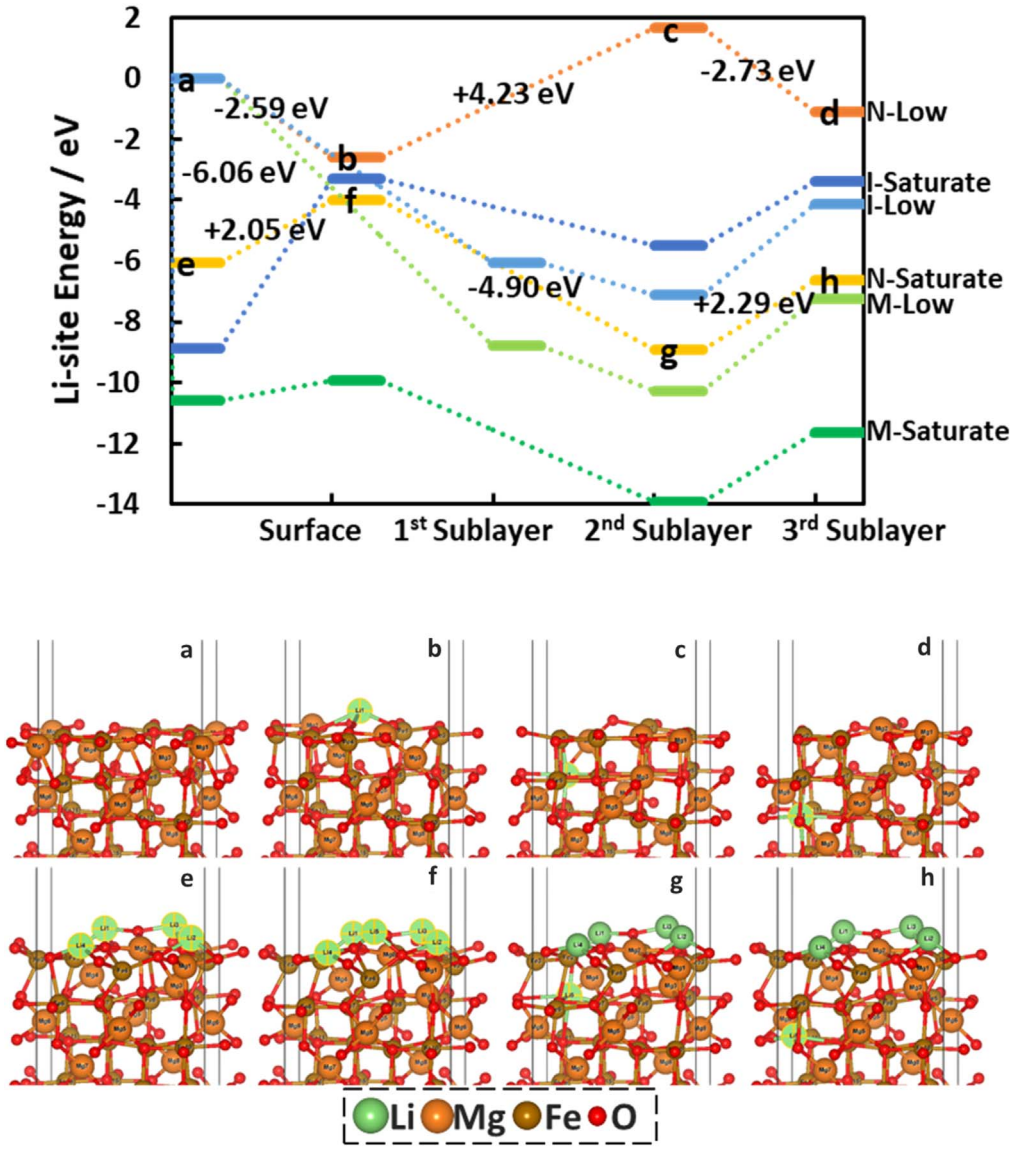

Figure 8. Top: energy profile of Li^+ transport from normal-spinel $MgFe_2O_4$(1 0 0)-Mg, mixed-spinel (1 0 0)-$Mg_{1.5}Fe_{1.5}O_4$ and inverse-spinel (0 0 1)-Mg_2FeO_4 surfaces to subsurface at low and saturate coverage, where the energy was expressed with respect to bare surface and aqueous Li^+ ion. (N-: normal-spinel, M-: mixed-spinel, I-: inverse-spinel) Bottom: the corresponding structures. a: bare (1 0 0)-Mg; b: Li^+ adsorption on (1 0 0)-Mg at low coverage; c: Li^+ transport to the 2nd sublayer at low coverage; d: Li^+ transport to the 3rd sublayer at low coverage; e: (1 0 0)-Mg saturated by Li^+; f: Li^+ adsorption on (1 0 0)-Mg at saturate coverage; g: Li^+ transport to the 2nd sublayer at saturate coverage; h: Li^+ transport to the 3rd sublayer at saturate coverage.

saturate coverage. Again, at low coverage the initial Li^+ adsorption on 16c-Vacancy site at the 1st layer (−6.07 eV, Figs. S8a, S8b) and the transport to the 2nd sublayer (−1.07 eV, Fig. S8c) are both downhill; while the displacement from the 2nd to the 3rd sublayer is uphill (3.01 eV). At saturation coverage, the Li^+ ion adsorption is highly hindered ($E_b = 5.56$ eV); while the sequential transport to the 2nd sublayer (−2.18 eV) is more favorable.

According to our DFT calculations, upon electrochemical discharge the stable $MgFe_2O_4${1 0 0} surfaces in three spinel structures are likely saturated by Li^+ ions first, which is followed by the Li^+ transport from the surface to subsurface. All saturated surfaces studied feature an endothermic adsorption of Li^+ ion on the surface, a sequential exothermic transport to the 2nd sublayer and eventually an uphill transport to the 3rd sublayer. Wherein the 16c-Vacancy site is preferred in the sublayers in all cases. Energetically, the mixed-spinel (1 0 0)-$Mg_{1.5}Fe_{1.5}O_4$ displays the lowest endothermicity along the adsorption and transport path (Fig. 7), which is followed by the inverse-spinel (0 0 1)-Mg_2FeO_4 and the normal-spinel (1 0 0)-Mg in a decreasing sequence. Overall, the mixed-spinel (1 0 0)-$Mg_{1.5}Fe_{1.5}O_4$ surface is the most active among the diverse $MgFe_2O_4$ surfaces studied, which likely displays the high capacity, the high voltage and Li^+ transport at initial discharging stage. Our study implies that the controlled synthesis toward maximization of such facet should enable a significant promotion in stability and discharge performance of $MgFe_2O_4$.

Conclusions

We employed DFT to study the contributions from diverse facets of $MgFe_2O_4$ in three spinel structures, normal-spinel, mixed-spinel and inverse-spinel, to the discharge performance, where various stable surfaces were considered, including normal-spinel (1 0 0) and (3 1 1), mixed-spinel {1 0 0}, inverse-spinel (1 0 0), (0 0 1), (1 1 1) and (3 1 1). Our results show that at the initial stage the Li^+ prefers to accumulate on all the surfaces to saturated coverage before transport to subsurface.

Among the surfaces studied, the mixed-spinel (1 0 0)-$Mg_{1.5}Fe_{1.5}O_4$ is likely the most active, being able to take advantage of the normal-spinel and the inverse-spinel. It can provide high capacity via accommodation of large amount of Li^+ ions, as seen for the normal-spinel (1 0 0)-Mg. In the meantime, the high voltage and Li^+ transport at initial discharging stage are also maintained via the high capability to capture Li^+ ions on the surface and the enabled smooth transport from surface to subsurface, similarly as inverse-spinel (0 0 1)-Mg_2FeO_4. Notably, the discharge voltages estimated based on the mixed-spinel (1 0 0)-$Mg_{1.5}Fe_{1.5}O_4$ fit well with the corresponding experimental measurements at the initial stage, which are greatly underestimated using the stoichiometric $MgFe_2O_4$ bulk model. Our results highlight the importance of density of surface Mg^{2+} in controlling the performance of $MgFe_2O_4$ surface during lithiation. It should be moderate, as mixed-spinel (1 0 0)-$Mg_{1.5}Fe_{1.5}O_4$, being low enough to enable the accumulation of Li^+ ions and thus high capacity, but high enough to ensure the high voltage and Li^+ transport together with reasonable stability. Such in-depth mechanistic understanding can open a new design strategy towards optimizing the particle morphology to improve the stability, the capacity, the discharge potential and Li^+ transport of ferrites as LIB electrode.

Acknowledgments

This work was carried out at Brookhaven National Laboratory (BNL). This work was funded as part of the Center for Mesoscale Transport Properties (m2M t−1), an Energy Frontier Research Center (EFRC) supported by the U.S. Department of Energy, Office of Science, Basic Energy Sciences, under Award No. DE-SC0012673. MRCAT operations are supported by the Department of Energy and the MRCAT member institutions. The DFT calculations were performed using computational resources at the Center for Functional Nanomaterials, which is a U.S. DOE Office of Science Facility, at Brookhaven National Laboratory under Contract No. DE-SC0012704, and the Scientific Data and Computing Center, a component of the BNL Computational Science Initiative. E.S.T. acknowledges William and Jane Knapp for support as the William and Jane Knapp Chair in Energy and the Environment.

ORCID

Ping Liu https://orcid.org/0000-0001-8363-070X

References

1. S. Yuvaraj, R. K. Selvan, and Y. S. Lee, *RSC Adv.*, **6**, 21448 (2016).
2. Y. Zhang, C. J. Pelliccione, A. B. Brady, H. Guo, P. F. Smith, P. Liu, A. C. Marschilok, K. J. Takeuchi, and E. S. Takeuchi, *Chem. Mater.*, **29**, 4282 (2017).
3. H. Guo, Y. Zhang, A. C. Marschilok, K. J. Takeuchi, E. S. Takeuchi, and P. Liu, *Phys. Chem. Chem. Phys.*, **19**, 26322 (2017).
4. H. Guo, A. C. Marschilok, K. J. Takeuchi, E. S. Takeuchi, and P. Liu, *ACS Appl. Mater. Interfaces*, **10**, 35623 (2018).
5. D. Bock et al., *ACS Appli. Energy Mater.* (2020), Submitted.
6. C. N. Lininger, C. A. Cama, K. J. Takeuchi, A. C. Marschilok, E. S. Takeuchi, A. C. West, and M. S. Hybertsen, *Chem. Mater.*, **30**, 7922 (2018).
7. H. Guo, A. C. Marschilok, K. J. Takeuchi, E. S. Takeuchi, and P. Liu, *Adv. Mater. Interfaces*, **6**, 1901218 (2019).
8. C. Liu, B. Zou, A. J. Rondinone, and Z. J. Zhang, *J. Am. Chem. Soc.*, **122**, 6263 (2000).
9. V. Šepelák, D. Baabe, F. J. Litterst, and K. D. Becker, *J. Appl. Phys.*, **88**, 5884 (2000).
10. M. Gateshki, V. Petkov, S. K. Pradhan, and T. Vogt, *J. Appl. Cryst.*, **38**, 772 (2005).
11. P. Holec, J. Plocek, D. Nižňanský, and J. P. Vejpravová, *J. Sol-Gel Sci. Technol.*, **51**, 301 (2009).
12. N. Sivakumar, A. Narayanasamy, J. M. Greneche, R. Murugaraj, and Y. S. Lee, *J. Alloys Compd.*, **504**, 395 (2010).
13. S. Da Dalt, A. S. Takimi, T. M. Volkmer, V. C. Sousa, and C. P. Bergmann, *Powder Technol.*, **210**, 103 (2011).
14. S. Permien, S. Indris, M. Scheuermann, U. Schürmann, V. Mereacre, A. K. Powell, L. Kienle, and W. Bensch, *J. Mater. Chem. A*, **3**, 1549 (2015).
15. B. Zheng, S. Wu, X. Yang, M. Jia, W. Zhang, and G. Liu, *ACS Appl. Mater. Interfaces*, **8**, 26683 (2016).
16. J. Guo, L. Shi, L. Wu, S. Pan, X. Yuan, and J. Zhao, *Mater. Res. Express*, **5**, 126301 (2018).
17. Y. Hou, F. Zuo, A. Dagg, and P. Feng, *Angew. Chem. Int. Ed.*, **52**, 1248 (2013).
18. A. K. Rai, T. V. Thi, J. Gim, and J. Kim, *Mater. Charact.*, **95**, 259 (2014).
19. Y. Liu, P. Zhang, M. Fan, and P. Jiang, *Fuel*, **164**, 314 (2016).
20. Y. Pan, Y. Zhang, X. Wei, C. Yuan, J. Yin, D. Cao, and G. Wang, *Electrochim. Acta*, **109**, 89 (2013).
21. Y. Guo, G. Qin, E. Liang, M. Li, and C. Wang, *Ceram. Int.*, **43**, 12519 (2017).
22. V. K. Tripathi and R. Nagarajan, *Adv. Powder Technol.*, **27**, 1251 (2016).
23. Y. Zu, Y. Zhao, K. Xu, Y. Tong, and F. Zhao, *Ceram. Int.*, **42**, 18844 (2016).
24. G. Kresse and J. Furthmüller, *Phys. Rev. B*, **54**, 11169 (1996).
25. G. Kresse and D. Joubert, *Phys. Rev. B*, **59**, 1758 (1999).
26. V. I. Anisimov, J. Zaanen, and O. K. Andersen, *Phys. Rev. B*, **44**, 943 (1991).
27. V. I. Anisimov, F. Aryasetiawan, and A. I. Lichtenstein, *J. Phys. Condens. Matter*, **9**, 767 (1997).
28. S. L. Dudarev, G. A. Botton, S. Y. Savrasov, C. J. Humphreys, and A. P. Sutton, *Phys. Rev. B*, **57**, 1505 (1998).
29. P. E. Blöchl, *Phys. Rev. B*, **50**, 17953 (1994).
30. J. P. Perdew, K. Burke, and M. Ernzerhof, *Phys. Rev. Lett.*, **77**, 3865 (1996).
31. R. Dom, R. Subasri, K. Radha, and P. H. Borse, *Solid State Commun.*, **151**, 470 (2011).
32. S. J. Mole, X. Zhou, and R. Liu, *J. Phys. Chem.*, **100**, 14665 (1996).
33. M. K. Aydinol, A. F. Kohan, and G. Ceder, *Phys. Rev. B*, **56**, 1354 (1997).
34. S. Ilhan, S. G. Izotova, and A. A. Komlev, *Ceram. Int.*, **41**, 577 (2015).
35. J. Nonkumwong, S. Ananta, P. Jantaratana, S. Phumying, S. Maensiri, and L. Srisombat, *J. Magn. Magn. Mater.*, **381**, 226 (2015).
36. A. Loganathan and K. Kumar, *Applied Nanoscience*, **6**, 629 (2015).
37. J. I. Langford and A. J. C. Wilson, *J. Appl. Crystallogr.*, **11**, 102 (1978).
38. A. L. Patterson, *Phys. Rev.*, **56**, 978 (1939).
39. S. M. Antao, I. Hassan, W. A. Crichton, and J. B. Parise, *Am. Mineral.*, **90**, 1500 (2005).
40. C. Gong, Y. J. Bai, Y. X. Qi, N. Lun, and J. Feng, *Electrochim. Acta*, **90**, 119 (2013).
41. H. Qiao, L. Luo, K. Chen, Y. Q. Fei, R. R. Cui, and Q. F. Wei, *Electrochim. Acta*, **160**, 43 (2015).
42. Y. Y. Hu et al., *Nat. Mater.*, **12**, 1130 (2013).
43. A. Ponrouch, P. L. Taberna, P. Simon, and M. R. Palacin, *Electrochim. Acta*, **61**, 13 (2012).
44. S. Laruelle, S. Grugeon, P. Poizot, M. Dolle, L. Dupont, and J. M. Tarascon, *J. Electrochem. Soc.*, **149**, A627 (2002).